Paper published in Cryogenics **133** (2023) 103693, https://doi.org/10.1016/j.cryogenics.2023.103693

Adapting a commercial integrated circuit 3-axis Hall sensor for measurements at low temperatures: mapping the three components of B in superconducting applications

N Rotheudt, J F Fagnard, P Harmeling and P Vanderbemden

Department of Electrical Engineering and Computer Science, Montefiore Institute B28, University of Liège, B-4000 Liège, Belgium

E-mail : Nicolas.Rotheudt@uliege.be

Abstract. Mapping the magnitude and the direction of the flux density $\vec{B}$ at cryogenic temperature is of particular interest in numerous applications involving superconductors. However, it is difficult to find 3-axis Hall probes or magnetometers operating at low temperature and above the mT range. In this work, we report the design and the construction of a device able to perform such a measurement. We show that it is possible to take advantage of a commercially available, inexpensive, room-temperature 3-axis Hall sensor and place it inside a thin cylindrical insert whose inner temperature is carefully controlled to be 25 ± 0.2°C, irrespective of the outer cryogenic temperature (typically 77 K). The active area of the Hall sensor is located at 2.2 ± 0.25 mm from the bottom of the insert, so that it can be positioned close to the magnetic structures to be characterized. We built the interfacing electronics that is located sufficiently close (typ. < 300 mm) to the digital Hall sensor and manages the temperature control. The whole system behaves thus as an independent and reliable 3-axis Hall probe able to operate in cryogenic conditions. We tested this device to characterize B_x, B_y and B_z generated by two magnetized high-T_c superconductors: a bulk polycrystalline tube and a ring magnet made from an eye-shaped coated conductor. We show that the device allows measurements down to ~ 0.16 mT. Combining the three measured components of $\vec{B}$ enables mapping the local magnitude and direction of the flux density.

Key words. 3-axis Hall sensor, cryogenic Hall probe, magnetic flux mapping, high-temperature superconductor, bulk superconductor, coated conductor.

1. Introduction

Nowadays, applications involving superconductors are of increasing complexity. Measuring the local magnetic flux density $\vec{B}$ inside or around a superconducting structure is often a key enabler towards the improvement of these applications. These include e.g. medical imaging [1], rotating machines [2-4], particle accelerators [5,6], power cables [7] or magnetic separation [8]. A well-established technique to characterize the flux density generated by a magnetized superconductor is to move a 1-axis Hall probe close to the superconducting device ('Hall probe mapping'). Most Hall sensors are sensitive to one component of the flux density, usually referred to as B_z. This technique has been used for around 30 years [9,10] to characterize superconductors of various forms, including tapes [11-13] or bulk samples, either single domains [14-16], multi-seeded [17] or foams [18]. Sub-millimetric resolution can be achieved [19] and Hall probes can be used up to several teslas [20]. However, being able to measure simultaneously the three components of the flux density brings an additional insight when the geometry is such that the lateral components B_x and B_y cannot be easily deduced from B_z. Such a situation occurs e.g. when several bulk superconductors are used in a rotating machine [21] or arranged to generate a well-defined space-dependent field [22,23]. In addition, a 3-axis measurement can easily handle situations where superconductors are subjected to non-homogeneous fields, e.g. in magnetic levitation systems [24], or when the shape of the flux lines is modified by ferromagnets [25]. Using a 3-axis measurement system also allows mappings over non-planar geometries to be performed, by combining mathematically the three measured components [26]. In this paper, we focus on the problem of measuring simultaneously the spatial distribution of B_x, B_y and B_z at cryogenic temperature (typically 77 K) with a measurement device able to accommodate relatively large samples (a few cm and above) and to operate for flux densities above the mT range, which is suitable for several high-temperature superconducting applications. Figure 1 shows schematically a few examples of situations that can be handled with the device described in this paper: (a) persistent current or electromagnets with a non-axisymmetric shape, e.g. eye-shaped loops or racetrack coils, (b) several bulk superconductors, e.g. placed in the rotor of a rotating machine, (c) investigation of inhomogeneous superconducting properties or defects, e.g. the presence of grain boundaries, (d) inhomogeneous applied fields produced e.g. by guideways for levitating systems at low temperature, (e) mapping the flux density around a non-planar device.

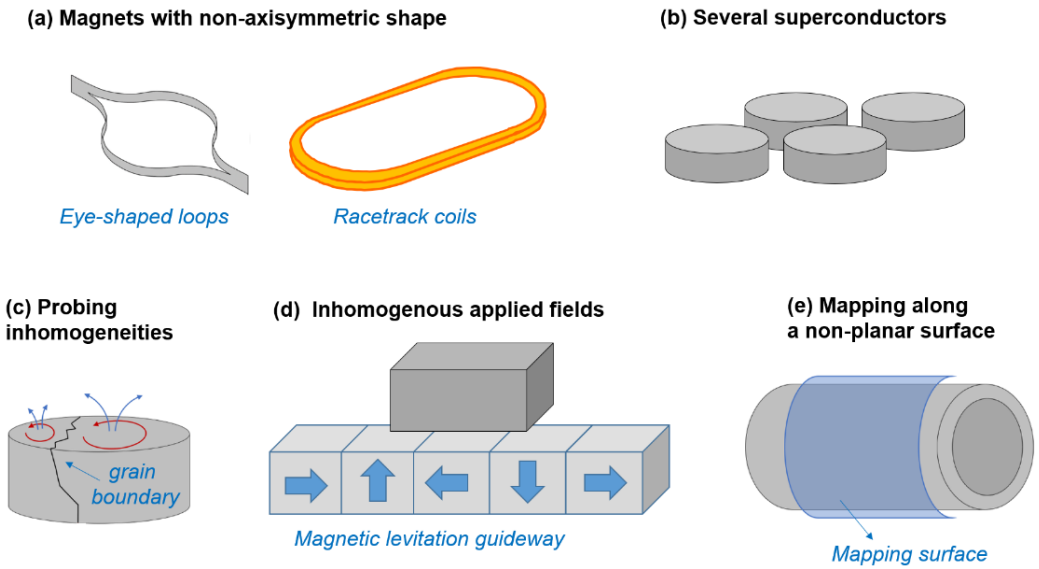

Fig. 1. Schematic examples of situations where a 3-axis Hall probe gives useful and additional information compared to a 1-axis Hall probe.

There exist a few ways to measure the three components of the magnetic flux density $\vec{B}$ in cryogenic conditions. First, fluxgate magnetometers can be used [27] and are commercially available. Their maximum operating range is, however, typically below 1 mT (e.g. ± 500 µT for Barington Instruments, CryoMag), which is well below the usual flux density in superconducting magnets. The second possibility is to use Superconducting QUantum Interference Device (SQUID) magnetometers for which progress in miniaturizing electronic devices allows the emergence of micro-scale SQUIDs sensitive to the local $\vec{B}$ [28]. Such systems are extremely sensitive and possess an outstanding resolution but their typical measurement range is well below 1 mT. Third, one can consider miniature Hall probes, i.e. with an active area of typically 0.01 mm². Their measurement range is usually between 100 µT and a few T. To obtain a 3-axis measurement, one can either combine mutually orthogonal cryogenic 1-axis Hall probes [29], at the expense of a loss in the spatial resolution, or use 3-axis, compact, cryogenic Hall probes (e.g. AREPOC, Axis-3). Such 3-axis probes were available in the past and could be used for the characterization of high-temperature superconducting structures [30-32]. However, while good quality 3-axis Hall sensors operating at room temperature are easy to find on the market (e.g. Melexis, MLX90395; Texas Instruments, TMAG5170-Q1; Metrolab, MagVector MV2; Allegro MicroSystems, ALS31313; STMicroelectronics, IIS2MDC), it is nowadays very difficult to find such components operating in cryogenic conditions. Using room-temperature Hall probes in cryogenic conditions has also been tried [33] with satisfying results in some cases [34] but the repeatability of such experiments was not reported.

In this work, we take advantage of a commercially available, inexpensive, integrated circuit (IC) 3-axis Hall sensor initially designed for non-contact Human Machine Interactions (HMI) applications at room temperature. The sensor is placed into a thin cylindrical insert (20 mm diameter) whose inner temperature is controlled to be as close as possible to 25°C, irrespective of the outer cryogenic temperature, here 77 K. The whole system then behaves as an independent and reliable 3-axis cryogenic Hall probe. The associated challenges that need to be overcome and that are addressed in this paper are the following. First, the distance between the active zone of the IC Hall sensor and the outer surface of the insert should be as small as possible. This is because the field generated by magnetized structures decays rapidly with the distance (typically $1/r^3$ with r the distance to the structure). Second, the temperature of the IC Hall sensor should never go below the absolute minimum operating temperature (typically -40°C) to prevent irreversible damage. Third, due to the possible small temperature dependence of the IC Hall sensor characteristics, its temperature should be controlled carefully. Finally, the output of most commercial IC 3-axis Hall sensors is digital. The output data are usually sent via Serial Peripheral Interface (SPI) or Inter-Integrated Circuit (I^2C), two protocols that should be used over a distance of few tens of centimetres at most [35]. The designed system should, therefore, include electronics placed close to the IC Hall sensor to process the data and convert them into a communication protocol ensuring a robust transmission over several metres, i.e. the typical distance between the cryogenic experiment and the computer.

2. Building the device

We designed a cylindrical insert whose bottom part is schematically shown in Fig.2. The objective is that the IC Hall sensor, placed as close as possible to the bottom outer surface, is kept at room temperature when the whole system is immersed in a liquid nitrogen bath.

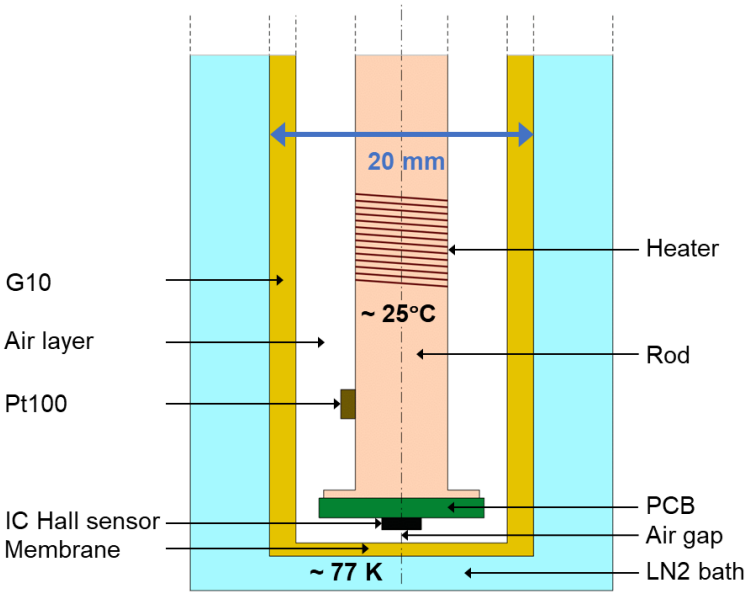

Fig. 2. Schematic illustration (cross-section) of the bottom part of the insert. To scale.

2.1. Design of the insert

The cylindrical enclosure of the insert (20 mm outer diameter, 16 mm inner diameter) is made of G10 epoxy resin (abbreviated G10 in the following), closed on the bottom side by a 1 mm-thick G10 membrane. The inner part consists of a 7 mm-diameter copper rod, electrically grounded. The copper rod accommodates a 12.5-mm diameter printed circuit board (PCB) holding the IC Hall sensor, as shown in Fig. 3. In order to ensure a good thermal contact between the Hall sensor and the copper rod, the PCB includes star-shaped copper pad, referred to as 'thermal plane'. This thermal plane is thermally anchored (i) to the thermal pad of the Hall probe through thermal vias, and (ii) to the copper rod itself through four thin (~ 0.6 mm-thick) legs, as shown in Fig. 4. Importantly, thermal insulation between the G10 enclosure and the central part is achieved through an air layer (~ 4.5 mm on the lateral side, and 1 mm between the bottom membrane and the Hall probe), as shown in Fig. 2. Preliminary temperature measurements inside the insert immersed in liquid nitrogen showed that both sides of the G10 membrane are at ~ 77 K; hence, the temperature gradient is mostly taken up by the air layer.

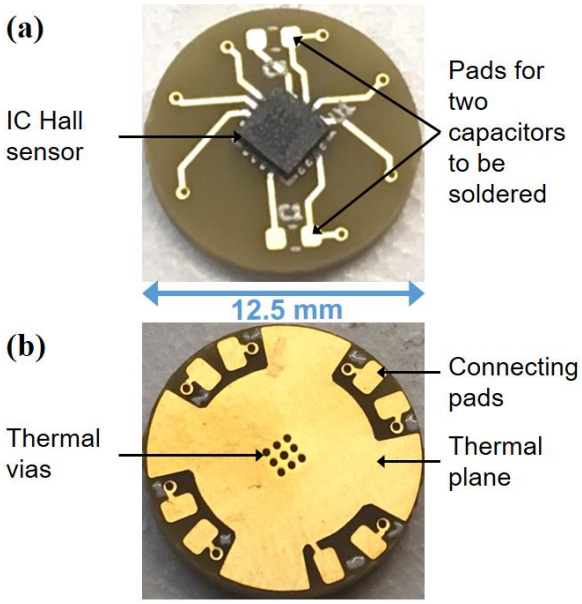

Fig. 3. Photographs showing both sides of the printed circuit board (PCB) holding the IC Hall sensor before being soldered to the rod. **(a)** The sensor is soldered at the centre of the PCB and two capacitors are added for filtering purposes. **(b)** The thermal plane is connected through thermal vias to the thermal pad of the IC Hall sensor. Connecting pads are placed to access the Hall sensor pins.

A 50 Ω heater, made of 100 µm-diameter constantan wire (55% Cu - 45% Ni, from Goodfellow) is wound anti-inductively around the copper rod (partly shown in Fig. 4). Even though it contains nickel, this heater, placed at ~ 20 mm from the Hall probe, is very unlikely to modify the $\vec{B}$ lines and alter the measurement. This is due to the low magnetic susceptibility of constantan [36] (10.83×10^{-6}) and the very small volume involved (< 6.3 mm³). A Pt100 temperature sensor (Innovative Sensor Technology, P0K1.232.6W.A.010) is attached with Kapton sheets on the copper rod ~ 10 mm above the Hall probe (Fig. 4).

The insert is closed by ISO-KF-16 components and the top part is machined from polyvinyl chloride (PVC) material. Sealed connectors are used for the connection wires. A sealed enclosure allows using dry air to reduce the risk of moisture condensation and freezing if needed. In addition, the insert can be connected to a vacuum pump. Preliminary experiments showed that using a high vacuum inside the enclosure (pressure < 1 mPa) reduces to almost zero the power requirement in the heater, at the expense of a system which becomes less practical. All experiments described below are therefore carried out at atmospheric pressure with no vacuum pump. The resulting device is shown in Fig. 5.

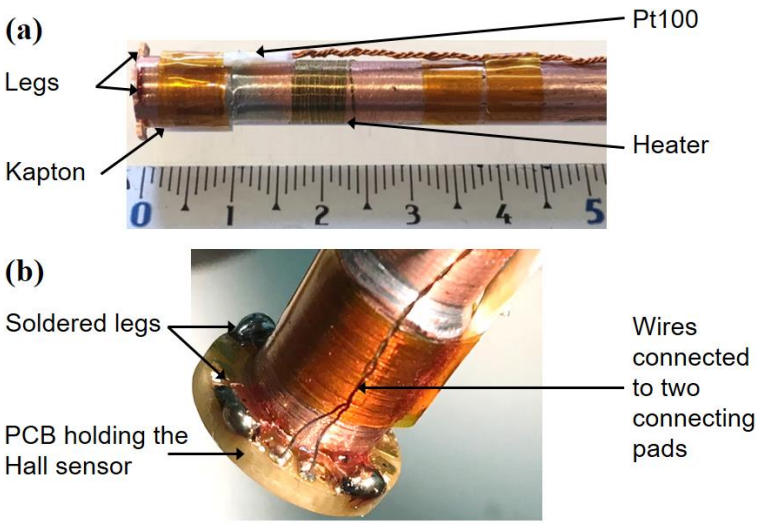

Fig. 4. Photographs showing the bottom part of the copper rod. **(a)** The legs, the Pt100 and the heater are visible. **(b)** The printed circuit board (PCB) holding the Hall sensor is soldered to the rod and two of the wires are connected to the pads, hence to the pins of the IC Hall sensor.

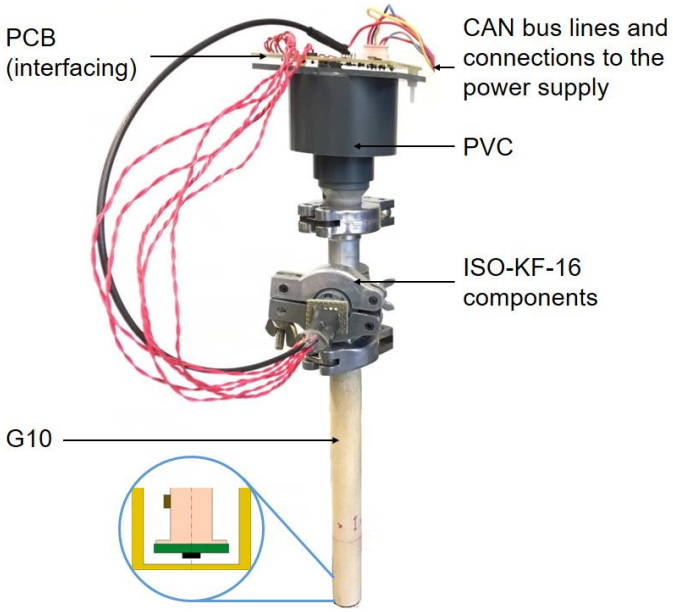

Fig. 5. Photograph of the overall system showing the insert, the interfacing PCB, the sealed connectors and the electric connections including the CAN (Controller Area Network) bus lines. The zoom circled in blue schematically shows the position of the IC Hall sensor inside the enclosure (see Fig. 1).

2.2 Electronic board for data processing and temperature control

The commercial 3-axis IC Hall sensor used in this device is the MLX90395 component, from Melexis. The Hall sensor uses a Triaxis® system based on eight Hall elements arranged on a circle with a radius of 250 µm [37]. The specifications of this commercial sensor at room temperature were first verified carefully using the procedure and metrics described in Appendix I. The typical uncertainty is around ± 200 µT for x and y and ± 100 µT for z. The average offsets and hysteresis for the three directions are of the order of the typical uncertainty. The integral non-linearity over a 100 mT measurement range is less than 700 µT. Interestingly, the probe response is linear over a more extended range than that guaranteed by the manufacturer: around ± 159 mT for x and y and ± 217.5 mT for z. The temperature dependence of the IC Hall sensor specifications between 5 and 65°C was investigated using the procedure and metrics given in Appendix II. The temperature coefficient of the Hall probe sensitivity is always found to be below 6×10^{-4} K^{-1}. The practical conclusion is that to guarantee e.g. a temperature-induced error of < 0.1%, the temperature stability of the Hall probe should be better than ~ 1.6°C.

Since the 16-bit output data of the IC Hall sensor are sent via Serial Peripheral Interface (SPI), the distance over which data are transmitted should be limited, typically < 300 mm. For this purpose, we designed an interfacing printed circuit board (PCB) located on top of the insert containing the Hall probe, i.e. outside liquid nitrogen. The microcontroller (Microchip Technology, PIC18F26K83) of this interfacing PCB is then connected via Controller Area Network (CAN) bus to a computer which runs an acquisition program (e.g. LabView). The CAN protocol can easily carry data over a few metres [38,39].

The interfacing PCB is fed by a double power supply (Manson, EP-613): 20 V / 0 V for the heating system and 12 V or 9 V / 0 V for the other components. A linear drop-out regulator is used to provide a stable voltage supply to the microcontroller. The PCB contains a Howland current source to deliver the fixed current (2 mA) to the Pt100 temperature sensor. The voltage drop across the Pt100 is measured via a 12-bit Analog-to-Digital Converter (ADC) embedded in the microcontroller. Appropriate filters and output impedance for the CAN bus are included via a transceiver circuit.

In order to keep the IC Hall sensor within its temperature operating range, we implemented a built-in temperature controller that is run by the microcontroller of the interfacing PCB. Preliminary experiments showed that, around room temperature, the temperature measured by the Hall probe internal sensor follows within ~ 0.5°C the temperature measured by the Pt100. In our design, the temperature measured by the internal sensor of the Hall probe (resolution = 0.02°C) is taken as the input of the controller. The Pt100 temperature offers useful redundancy and serves as a security check. As an output, the temperature controller sets the duty cycle of a Pulse Width Modulation (PWM) signal, which feeds the gate of a

MOSFET transistor (Nexperia, PMV20XNE). This MOSFET is connected in series with the constantan heater and the 20 V power supply. Hence, the power injected into the heater ranges between 0 W and 8 W. The built-in temperature controller is proportional integral (PI). The setpoint temperature is 25°C. The P and I parameters of the controller are tuned using the Ziegler-Nichols method [40]. Special care is taken to avoid the so-called integrator windup problem [41] that may occur when the requested power should go beyond the physical limits (0 or 8 W) and therefore saturates; when this happens the integration of the controller stops. Also, security states are implemented to avoid the temperature of the system to go below 5°C or above 50°C. The sequence of the tasks performed by the microcontroller is listed in Appendix III.

3. Characteristics of the constructed device

In this section we aim at characterizing (i) the exact distance between the active zone of the IC Hall sensor and the outer surface of the insert and (ii) the efficiency of the designed temperature controller when the system is immersed in the liquid nitrogen.

3.1. Position of the Hall probe within the insert

We first determine experimentally the distance between the bottom outer side of the insert (Fig. 2) and the active region of the IC Hall sensor. In theory, this distance is $z_{\mathrm{HS}}^{\mathrm{th}} \sim 2.4$ mm, corresponding to the sum of the thickness of the G10 membrane (1 mm), the air gap ($\sim$ 1 mm) and the location of the active region within the IC Hall sensor (0.4 mm, according to manufacturer data). When immersed in liquid nitrogen, the thermal contraction of G10 enclosure with respect to its length at room temperature is estimated to be around 0.2% [42]. In a typical application, ~ 50 mm of G10 are immersed, leading to a change of the distance $z_{\mathrm{HS}}^{\mathrm{th}}$ of around 0.1 mm.

In order to measure the distance $z_{\mathrm{HS}}^{\mathrm{exp}}$ experimentally, the insert is attached to a *xyz* micro-positioning stage (Thorlabs, MTS50/M-Z8) and moved vertically along the axis of a solenoid air coil with steps of 0.25 mm, at room temperature. If z denotes the position along the axis of the coil, the flux density $B_z(z)$ exhibits a maximum at the centre of the coil $z = 0$ mm. Figure 6 shows B_z plotted as a function of z^*, the vertical position of the bottom of the G10 insert with respect to the centre of the coil. The $B_z(z^*)$ plot exhibits a maximum at $z_{\mathrm{max}}^* \neq 0$ mm, where $|z_{\mathrm{max}}^*|$ corresponds to $z_{\mathrm{HS}}^{\mathrm{exp}}$. In order to locate precisely the position of the maximum, second-order functions are used to fit different ranges of experimental data (shown in red in the inset in Fig. 6). This procedure yields $z_{\mathrm{HS}}^{\mathrm{exp}} = 2.2 \pm 0.25$ mm, where the uncertainty comes from both the limited resolution of the positioning stage and the exact range of data used for the second-order approximation. Given the targeted temperature difference (~ 220 K) between the active zone of the IC Hall

sensor and the cryogenic bath, this distance corresponds to an average temperature gradient of $\sim 100\ \mathrm{K/mm}$.

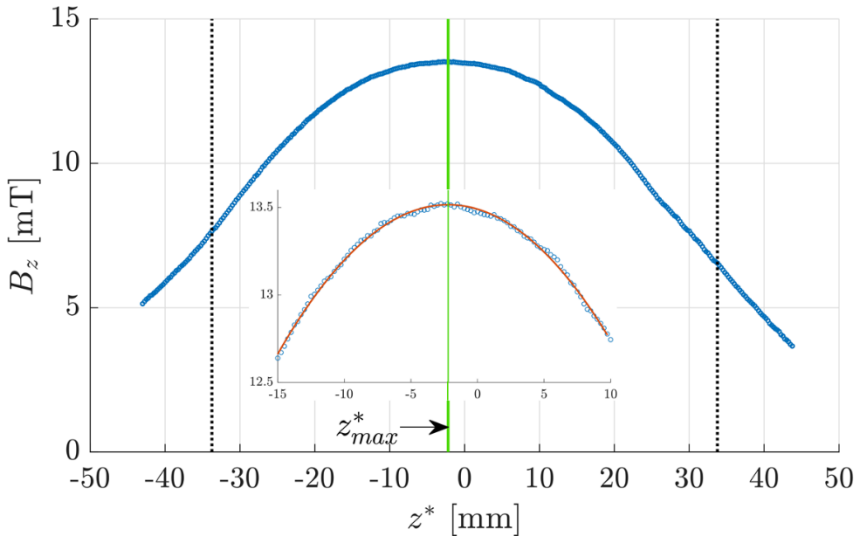

Fig. 6. Axial flux density measured by the IC Hall sensor as a function of z^*, the vertical position of the bottom of the G10 insert (blue). Inset: second-order function is fitted for a range of ± 12.5 mm around the experimental maximum (red). The maximum of this second-order function occurs for z^*_{max} (green). The dotted black lines indicate the positions of the openings of the coil.

3.2. Efficiency of the built-in temperature controller

To illustrate the performances of the built-in temperature controller, the following experiment is performed. At $t = 0$ s, the power supplies of the interfacing PCB are simultaneously turned on. Then, at $t \approx 60$ s, the bottom part of the insert is immersed in liquid nitrogen (77 K). The time evolution of the temperature as measured by the embedded temperature sensor of the Hall sensor is shown in Fig. 7(a). Figure 7(b) shows the time evolution of the power requested by the controller during the experiment.

First, the device is at room temperature (~ 22°C), which is slightly below the targeted 25°C. Hence, the controller requires a few watts to be injected into the heater, as can be observed for $t < 6$ s in Fig. 7(b). The temperature increases rapidly and stabilizes around 25°C after a few seconds (Fig. 7(a)). When the system is immersed in liquid nitrogen, at $t \approx 60$ s, the temperature quickly drops. The power injected into the heater then becomes purposely saturated at its maximum power (8 W). This behaviour is due to the relatively high proportional gain in the PI controller which ensures that the initial temperature dip after immersion is minimized. Figure 7(a) shows that the temperature controller counteracts the temperature drop very efficiently since the temperature of the Hall sensor is observed to never fall below 21°C. This experimental result is found to be perfectly reproducible.

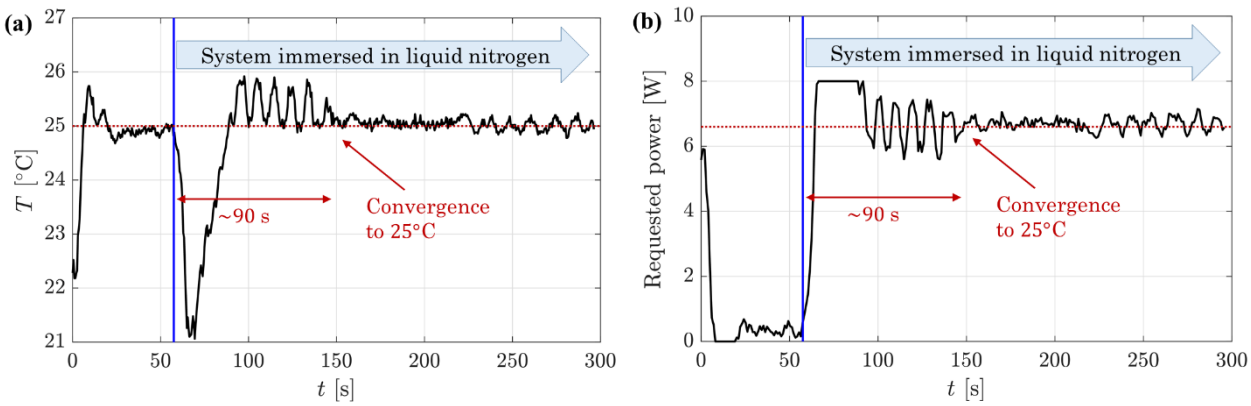

Fig. 7. (a) Time evolution of the temperature of the IC Hall sensor when the system is placed at room temperature before being immersed in liquid nitrogen after 60 s. **(b)** Time evolution of the power requested by the controller during the same experiment.

After the temperature dip, the relatively large injected power (8 W) is such that the temperature of the Hall sensor slightly exceeds 25°C. Between $t \approx 90$ s and $t \approx 150$ s, the requested power converges to ~ 6.6 W, which is the average power required to maintain the copper rod at room temperature while the system is immersed in liquid nitrogen. During that time, the temperature of the Hall sensor exhibits a few oscillations of total amplitude ~ 1°C, which are expected for such a PI controller [41]. Then, roughly 90 s after its immersion, i.e. at $t \approx 150$ s, the temperature of the system stabilizes at $25° \pm 0.2$°C. Given the upper bound of the temperature dependence of the Hall sensor sensitivity, the temperature oscillations yield an error < 0.012 %, i.e. much below the typical uncertainty. This ~ 90 s delay before stabilization is observed in all the experiments. Note that even during this time interval, the device can be used.

In summary, the above results show that the insert and the temperature controller designed in this work allow the commercial Hall sensor to be kept and safely operate around room temperature. These results enable the whole device to be used in cryogenic conditions down to $T = 77$ K.

4. Measurement examples and discussion

In this section we demonstrate the ability of the cryogenic 3-axis Hall probe designed in this work to measure the spatial distribution of B_x, B_y and B_z produced by two samples at 77 K: (i) a bulk superconducting tube and (ii) a ring magnet made of a second-generation coated conductor.

4.1. Bulk superconducting tube

The bulk superconducting tube is made of polycrystalline $Bi_2Sr_2Ca_2Cu_3O_{10}$ produced by the company 'CAN Superconductors' (critical temperature $T_c \approx 110$ K). The tube dimensions are: length $L = 20.8 \pm 0.1$ mm, inner radius $r_{in} = 10.6 \pm 0.1$ mm, outer radius $r_{out} = 12.3 \pm 0.1$ mm. First, the tube is immersed in liquid nitrogen and magnetized by an axial magnetic field ramped up to ~ 60 mT with a sweep rate of 1.2 mT/s. The applied field is then removed at the same rate. A sufficiently long time, typically 1 h, is elapsed to ensure that the relaxation of the induced currents in the superconductor (flux creep) is negligible during the duration of the experiments that follow.

In the first experiment (Fig. 8(a)), the 3-axis Hall probe is moved along the axis (z) of the tube with 1 mm steps to obtain $B_z(z)$. For each position, several data are averaged and the vertical error bars represent the standard deviation of these measurements, typically 100 μT. In the second experiment shown in the inset in Fig. 8(b), we map both the axial and radial fields in a plane above the superconducting tube, at $z = 15.3$ mm. The tube axis is located at $(x, y) = (0,0)$ and the mapping is performed from $(x, y) = (-20, -20)$ to $(20,20)$ [mm], with 2 mm steps. Figure 8(b) shows B_z in the xy mapping plane. A cut in this plane for $y = 0$ mm is shown in Fig. 8(c). In the latter, the dotted black lines indicate the position of the cross-section of the tube. The results show that the device is able to measure flux density values as low as ~ 0.16 mT, while the typical uncertainty is ± 100 μT.

Along the same cut, Fig. 8(d) shows the radial flux density B_r, as computed from B_x and B_y. The corresponding typical uncertainty on B_r is ± 200 μT. The measured flux density goes in this case as low as ~ 0.45 mT. This value is consistent with the small offsets observed for B_x and B_y (see Appendix I). The small dissymmetry of the curve with respect to $x = 0$ is likely to come from the inhomogeneity of the superconducting tube or a slight misalignment between the mapping plane and the top surface of the tube. Note that at low fields (1 mT or below), the typical noise level can possibly be decreased further by averaging a larger number of measurements, at the expense of an increased acquisition time.

These measurements can be exploited to estimate the critical current density of the permanently magnetized polycrystalline $Bi_2Sr_2Ca_2Cu_3O_{10}$ superconducting tube. Assuming that the tube is an infinitely thin solenoid of finite height L and radius $(r_{in} + r_{out})/2$ with an azimuthal supercurrent I, B_z at the centre of the tube writes

$$B_z(z = 0) = \frac{\mu_0 I}{2\sqrt{\left(\frac{L}{2}\right)^2 + \left(\frac{r_{in} + r_{out}}{2}\right)^2}}$$

Equating this formula with the experimental data for $B_z(0)$ yields a current $I \approx 113.5$ A, corresponding to a uniform current density of 3.2 MA/m². Note that this value underestimates the critical current density, since one hour was elapsed between the magnetization of the tube and the Hall probe mapping measurements. In addition, the $J_c(B)$ dependence, yielding a non-uniform distribution of J along the thickness, is neglected. In spite of these simplifying approximations, the current density obtained here is fully consistent with that obtained via Kim's law in a previous work [43]. The spatial distribution of B_z and B_r calculated analytically [44] from the current density are shown as dotted red lines in Fig. 8(a), (c) and (d) and are found to be fully consistent with the experimental data.

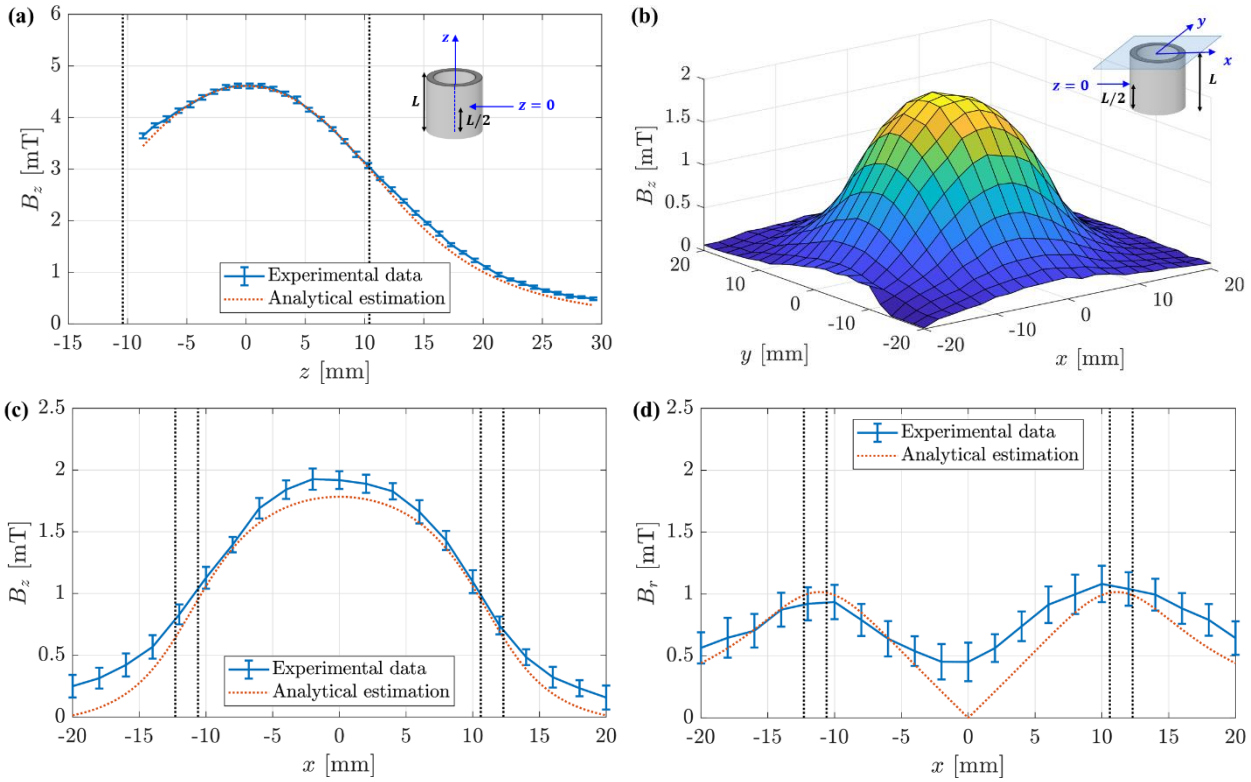

Fig. 8. (a) Measured and averaged B_z as a function of the position z along the tube axis (in blue). The dotted red line is an analytical estimation using $I = 113.5$ A. The dotted black lines indicate the positions of the openings of the tube. **(b)** Measured and averaged B_z as a function of both x and y (horizontal mapping) at $z = 15.3$ mm. **(c)** Cut in Fig. 8(b) for $y = 0$ mm (in blue). The error bars correspond to the standard deviation of the measurements. The dotted red line is an analytical estimation using $I = 113.5$ A. The dotted black lines show the position of the cross-section of the tube. **(d)** Same for the radial component $B_r = \sqrt{B_x^2 + B_y^2}$.

4.2 Ring magnet made of a second-generation coated conductor

Here, the cryogenic 3-axis Hall probe is used to measure the magnetic flux density components B_x, B_y and B_z produced by a superconductor whose geometry is not axisymmetric. The investigated structure is a superconducting 'eye-shaped loop' [45,46], as shown schematically in Fig. 9(a): a slit is milled in the middle of a coated conductor section in order to form a closed superconducting loop in which persistent currents can flow. Such a structure forms the basis for ring-shaped superconducting magnets made of coated conductors [47-52].

A 126 mm-long slit is cut along the centre line of three 10 mm × 154 mm sections of a second-generation $GdBa_2Cu_3O_7$ coated conductor tape (2G-HTS tape) from Shanghai Superconductor. Both sides of the cuts are extended around a 60 mm-diameter cylinder and the three sections are superimposed on three layers, such that the trapped flux density is large enough to significantly overcome the typical uncertainty of the probe. The resulting structure is cooled down to 77 K without applied field and then subjected to a field ramped from 0 to ~ 60 mT and back to 0, with an average sweep rate of 150 µT/s. One hour is then elapsed, to ensure that the relaxation of the induced persistent current loops in the superconductor is negligible. The experiment consists in moving the 3-axis Hall probe along y at $x = 27$ mm and $z = 10.7$ mm, i.e., off-centred above the superconducting loop, as shown schematically by the red line in Fig. 9(a). A measurement is taken every 0.25 mm. The three measured components B_x, B_y and B_z are shown as a function of the y position in Fig. 9(b). In addition, B_x, B_y and B_z are calculated analytically using Biot-Savart's law applied to an eye-shaped structure, assuming a uniform current (422 A) circulates in the permanently magnetized eye-shaped loop. The calculated components of the flux density are shown in Fig. 9(c). The analytical estimation is found to reproduce nicely the experimental results. The differences are most likely due to a possible, slight misalignment (< 3 °) between the axes of the Hall probe and the reference axes of the eye-shaped loop.

All the three components are found to be of comparable magnitude and not to exhibit any symmetry with respect to $y = 0$. From the experimental results, the local magnitude $|\vec{B}|$ of the flux density and its orientation, described by the angles ϕ and θ, can be computed at every position along the measurement line (Fig. 9(d) to (f)). Both the magnitude and the orientation of $\vec{B}$ are observed to vary significantly as a function of y. The results shown in Fig. 9 can therefore be used to design complex superconducting structures combining several ring-shaped magnets, e.g. with different orientations. This application highlights that combining the three measured components brings additional information that could not be deduced from data obtained with a 1-axis Hall probe.

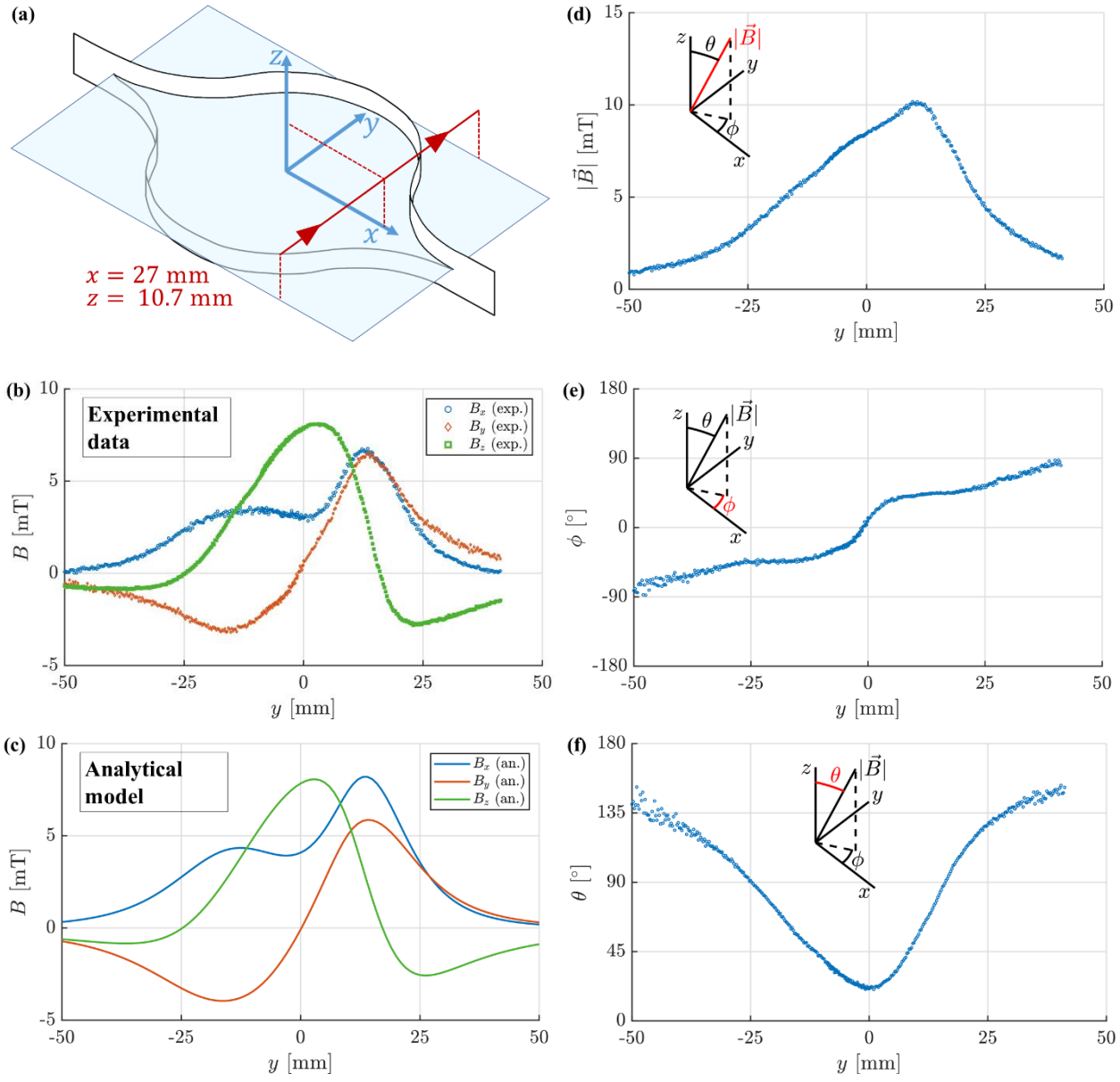

Fig. 9. (a) Schematic representation of an eye-shaped loop made by cutting a slit along the centre line of an eye-shaped loop made of 2G-HTS tape. The plane of the slit ($z = 0$) is in blue. The red line shows the trajectory followed by the 3-axis Hall probe during the experiment. **(b)** Measured magnetic flux density (B_x: blue circles, B_y: red diamonds, B_z: green squares). **(c)** Computed flux density using Biot-Savart's law. **(d)** Experimental magnitude of $\vec{B}$, i.e., $\sqrt{B_x^2 + B_y^2 + B_z^2}$. **(e)** and **(f)** Experimental angles (ϕ and θ) describing the local orientation of $\vec{B}$, as classically described by the spherical coordinates reminded in the insets. All values from graphs **(b)** to **(f)** are given as a function of y, for $x = 27$ mm and $z = 10.7$ mm.

5. Conclusion

We showed how to take advantage of a commercially available IC Hall sensor operating at room temperature to make an efficient, inexpensive cryogenic 3-axis Hall probe able to measure the spatial distribution of B_x, B_y and B_z at 77 K. We designed an insert to accommodate the IC Hall sensor and keep it at room temperature. The resulting device has the shape of a measuring rod whose outer diameter is 20 mm. Special care was taken to place the active area of the Hall sensor as close as possible to the bottom end of the device. Measurements show that this distance is 2.2 mm. Inside the insert, the Hall probe is thermally anchored to a copper rod whose temperature is carefully controlled. We designed the electronics, managing the data transfer to a computer. The electronics, which must be placed at reasonable distance from the Hall sensor, also include a built-in temperature controller aimed at keeping the Hall sensor at room temperature. As a result, the only devices needed are a DC power supply and a computer handling digital output data on a CAN bus or any other robust protocol. We demonstrated the successful operation of the temperature controller when the rod is immersed in liquid nitrogen. In spite of the close proximity of the Hall sensor with the bottom end, the temperature never falls below 21°C. The temperature can be stabilized at 25 ± 0.2°C after a delay of ~ 90 s following the immersion in the cryogenic bath. The 0.2°C temperature variation of the integrated circuit leads to a reading error that is much smaller than the typical uncertainty of the sensor.

The design of the insert combined to the efficient temperature control allows us to map the 3D magnetic flux density generated by superconducting structures, as an example, a bulk superconducting tube and a superconducting ring magnet ('eye-shaped loop'). This latter configuration is one of the various situations that benefits from a 3-axis measurement. The design of the 3-axis Hall probe is not restricted to the particular IC Hall sensor used and could be possibly applied to other Hall sensors having a larger operating range (e.g. a few teslas), if such components are available. Since 3-axis Hall probes operating in cryogenic conditions are no longer commercialized nowadays, the constructed device is particularly helpful to deepen our understanding of the magnetic behaviour of large superconducting structures and to improve their design.

Acknowledgments

This work was supported by the Fonds de la Recherche Scientifique - FNRS under grant CDR n° J.0218.20 (35325237). We are grateful to E. Lahaye and, through him, Melexis, for providing the IC Hall sensors. Nicolas Rotheudt is recipient of an FRS-FNRS Research Fellow grant.

References

[1] Thekkethil S R, Kar S, Kumar M, Soni V, Suman N V, Sharma R G, Rastogi V, Datta T S. Stress-Induced Magnetic Field Inhomogeneity in a 1.5 T Superconducting MRI Magnet. IEEE Trans Appl Supercond 2018; 28(4):4401905. *https://doi.org/10.1109/TASC.2018.2805170*

[2] Song X, Mijatovic N, Kellers J, Bührer C, Rebsdorf A V, Hansen J, Christensen M, Krause J, Pütz H, Wiezoreck J, Holbøll J. A Pole Pair Segment of a 2-MW High Temperature Superconducting Wind Turbine Generator. IEEE Trans Appl Supercond 2017; 27(4):1–5 *https://doi.org/10.1109/TASC.2017.2656778*

[3] Xu X, Huang Z, Li W, Huang X, Wang M, Hong Z, Jin Z. 3D finite element modelling on racetrack coils using the homogeneous T-A formulation. Cryogenics 2021; 119:103366 *https://doi.org/10.1016/j.cryogenics.2021.103366*

[4] Yang K, Zhang T, He J, Zhang Q, Zhang C, Zhou D, Cai C. Pulsed Field Magnetization of $YBa_2Cu_3O_{7-\delta}$ Bulk Assembly for Motor Application. IEEE Trans Appl Supercond 2022; 32(4):5200205 *https://doi.org/10.1109/TASC.2021.3133826*

[5] Petrone C, van Nugteren J, Bajas H, Bottura L, Kirby G, Rossi L, Russenschuck S. Measurement and Analysis of the Dynamic Effects in an HTS Dipole Magnet. IEEE Trans Appl Supercond 2018; 28(4):4604404 *https://doi.org/10.1109/TASC.2018.2801325*

[6] Bortot L, Mentink M, Petrone C, Van Nugteren J, Deferne G, Koettig T, Kirby G, Pentella M, Perez J C, Pincot F O, De Rijk G, Russenschuck S, Verweij A P, Schöps S. High-Temperature Superconducting Screens for Magnetic Field-Error Cancellation in Accelerator Magnets. Supercond Sci Technol 2021; 34(10):105001 *https://doi.org/10.1088/1361-6668/ac1c13*

[7] Obana T, Terazaki Y, Yanag N, Hamaguchi S, Chikaraishi H, Takayasu M. Self-field measurements of an HTS twisted stacked-tape cable conductor. Cryogenics 2020; 105:103012 *https://doi.org/10.1016/j.cryogenics.2019.103012*

[8] Kosse J J, Dhallé M, Tomás G, Rem P C, ter Brake H J M, ten Kate H H J. Optimum Coil-System Layout for Magnet-Driven Superconducting Magnetic Density Separation. IEEE Trans Magn 2021; 57(8):9000209 *https://doi.org/10.1109/TMAG.2021.3080178*

[9] Chen I G, Liu J, Weinstein R, Lau K. Characterization of $YBaCu_3O_7$, including critical current density J_c, by trapped magnetic field. J Appl Phys 1992; 72(3):1013–20. *https://doi.org/10.1063/1.351826*

[10] Nagashima K, Higuchi T, Sok J, Yoo S I, Fujimoto H, Murakami M. The Trapped Field of YBCO Bulk Superconducting Magnets. Cryogenics 1997; 37(10):577–81. *https://doi.org/10.1016/S0011-2275(97)00058-1*

[11] Solovyov M, Vojenciak M, Gömöry F. Magnetic Field Mapping Above the Superconducting Tape with Ni-Covered Edges. IEEE Trans Appl Supercond 2009; 19(3):3049–52. *https://doi.org/10.1109/TASC.2009.2019067*

[12] Leclerc J, Berger K, Douine B, Lévêque J. Field Mapping Measurements to Determine Spatial and Field Dependence of Critical Current Density in YBCO Tapes. Physica C 2013; 492: 158–64. *https://doi.org/10.1016/j.physc.2013.06.009*

[13] Tallouli M, Sun J, Chikumoto N, Otabe E S, Shyshkin O, Charfi-Kaddour S, Yamaguchi S. Observation of self-magnetic field relaxations in Bi2223 and Y123 HTS tapes after over-current pulse and DC current operation. Cryogenics 2016; 77:53-58. *https://doi.org/10.1016/j.cryogenics.2016.04.010*

[14] Cardwell D, Murakami M, Zeisberger M, Gawalek W, Gonzalez-Arrabal R, Eisterer M, Weber H, Fuchs G, Krabbes G, Leenders A, Freyhardt H, Chaud X, Tournier R, Hari Babu N. Round Robin Measurements of the Flux Trapping Properties of Melt Processed Sm-Ba-Cu-O Bulk Superconductors. Physica C 2004; 412-414:623–32. *https://doi.org/10.1016/j.physc.2004.01.082*

[15] Iliescu S, Sena S, Granados X, Bartolome E, Puig T, Obradors X, Carrera M, Amoros J, Krakunovska S, Habisreuther T. In-Field Hall Probe Mapping System for Characterization of YBCO Welds. IEEE Trans Appl Supercond 2003; 13(2):3136–39. *https://doi.org/10.1109/TASC.2003.812123*

[16] Chaud X, Noudem J, Prikhna T, Savchuk Y, Haanappel E, Diko P, Zhang C P. Flux Mapping at 77 K and Local Measurement at Lower Temperature of Thin-Wall YBaCuO Single-Domain Samples Oxygenated Under High Pressure. Physica C 2009; 469(15):1200–1206. *https://doi.org/10.1016/j.physc.2009.05.017*

[17] Shi Y, Dennis A R, Zhou D, Namburi D K, Huang K, Durrell J H, Cardwell D A. Factors Affecting the Growth of Multiseeded Superconducting Single Grains. Cryst Growth Des 2016; 16(9):5110–17. *https://doi.org/10.1021/acs.cgd.6b00685*

[18] Koblischka M R, Pavan Kumar Naik S, Koblischka-Veneva A, Murakami M, Gokhfeld D, Reddy E S, Schmitz G J. Superconducting YBCO Foams as Trapped Field Magnets. Materials 2019; 12(6):853. *https://doi.org/10.3390/ma12060853*

[19] Higashikawa K, Inoue M, Ye S, Matsumoto A, Kumakura H, Yoshida R, Kato T, Machi T, Ibi A, Izumi T, Kiss T. Scanning Hall-probe microscopy for site-specific observation of microstructure in superconducting wires and tapes for the clarification of their performance bottlenecks. Supercond Sci Technol 2020;33:064005 *https://doi.org/10.1088/1361-6668/ab89ef*

[20] Myers C S, Sumption M D, Collings E W. Magnetization and Flux Penetration of YBCO CORC Cable Segments at the Injection Fields of Accelerator Magnets. IEEE Trans Appl Supercond 2019; 29(5):4701105. *https://doi.org/10.1109/TASC.2019.2896625*

[21] Dorget R, Nouailhetas Q, Colle A, Berger K, Sudo K, Ayat S, Lévêque J, Koblischka MR, Sakai N, Oka T, Douine B. Review on the Use of Superconducting Bulks for Magnetic Screening in Electrical Machines for Aircraft Applications. Materials 2021; 14(11):2847. *https://doi.org/10.3390/ma14112847*

[22] Kii T, Kinjo R, Kimura N, Shibata M, Bakr M A, Choi Y W, Omer M, Yoshida K, Ishida K, Komai T, Shimahashi K, Sonobe T, Zen H, Masuda K, Ohgaki H. Low-Temperature Operation of a Bulk HTSC Staggered Array Undulator. IEEE Trans Appl Supercond 2012; 22(3):4100904. *https://doi.org/10.1109/TASC.2011.2180498*

[23] Calvi M, Ainslie M D, Dennis A, Durrell J H, Hellmann S, Kittel C, Moseley D A, Schmidt T, Shi Y and Zhang K. A GdBCO bulk staggered array undulator. Supercond Sci Technol 2020; 33(1):014004. *https://doi.org/10.1088/1361-6668/ab5b37*

[24] Wang L, Deng Z, Cheng Y. A field cooling method to increase the suspension force of HTS pinning maglev system. Cryogenics 2022; 123:103448 *https://doi.org/10.1016/j.cryogenics.2022.103448*

[25] Chen W, Jin R, Wang S, Xu M, Che T, Shen B, Yang X, Zhao Y. The effect of flux diverters on the AC loss of REBCO coil coupled with iron core. Cryogenics 2022; 128:103573 *https://doi.org/10.1016/j.cryogenics.2022.103573*

[26] Hogan K, Fagnard J F, Wéra L, Vanderheyden B, Vanderbemden P. Magnetic Shielding of an Inhomogeneous Magnetic Field Source by a Bulk Superconducting Tube. Supercond Sci Technol 2015; 28 (3):035011. *https://doi.org/10.1088/0953-2048/28/3/035011*

[27] Lipovský P, Draganová K, Novotňák J, Szőke Z, Fil'ko M. Indoor Mapping of Magnetic Fields Using UAV Equipped with Fluxgate Magnetometer. Sensors 2021; 21(12):4191. *https://doi.org/10.3390/s21124191*

[28] Vu T D, Ho T H, Miyajima S, Toji M, Ninomiya Y, Shishido H, Maezawa M, Hidaka M, Hayashi M, Kawamata S, Ishida T. SQUID Microscopy for Mapping Vector Magnetic Fields. Supercond Sci Technol 2019; 32(11):115006. *https://doi.org/10.1088/1361-6668/ab3945*

[29] Kvitkovic J, Majoros M. Three-Axis Cryogenic Hall Sensor. J Magn Magn Mater 1996; 157-158:440–41 *https://doi.org/10.1016/0304-8853(95)01221-4*

[30] Paasi J, Kalliohaka T, Korpela A, Soderlund L, Hermann P F, Kvitkovic J, Majoros M. Homogeneity studies of multifilamentary BSCCO tapes by three-axis Hall sensor magnetometry. IEEE Trans Appl Supercond 1999; 9:1598–1601. *https://doi.org/10.1109/77.784702*

[31] Wéra L, Fagnard J-F, Levin G A, Vanderheyden B, Vanderbemden P. A Comparative Study of Triaxial and Uniaxial Magnetic Shields Made Out of YBCO Coated Conductors. Supercond Sci Technol 2015; 28(7):074001. *https://doi.org/10.1088/0953-2048/28/7/074001*

[32] Bruce R, Soulerin S, Bouziat D, Cubizolles R, Gastineau B, Juster F-P, Bredy P. Compact cryogenic test stand for superconducting magnets characterization. IOP Conf Ser: Mater Sci Eng 2020; 755(1):012147. *https://doi.org/10.1088/1757-899X/755/1/012147*

[33] González-Jorge H, Quelle I, Carballo E, Domarco G. Working with non-cryogenic Hall sensors at 77 K. Cryogenics 2006 ;46(10):736–39. *https://doi.org/10.1016/j.cryogenics.2006.06.005*

[34] Metrolab. Cool measurements with MagVector™ MV2, *https://www.metrolab.com/cool-measurements-with-magvector-mv2/*; 2019 [accessed 4 March 2023].

[35] Leens, F. An Introduction to I²C and SPI Protocols. IEEE Instrum Meas Mag 2009; 12(1):8–13. *https://doi.org/10.1109/MIM.2009.4762946*

[36] Williams E H. Magnetic Properties of Copper-Nickel Alloys. Phys Rev 1931; 38(4):828–31.

[37] Huber S, Burssens J-W, Dupré N, Dubrulle O, Bidaux Y, Close G, Schott C. A Gradiometric Magnetic Sensor System for Stray-Field-Immune Rotary Position Sensing in Harsh Environment. Proceedings of Eurosensors 2018; 2(13):809. *https://doi.org/10.3390/proceedings2130809*

[38] Rachid A, Collet F. 2020. Bus CAN. Techniques de l'ingénieur: Automatique et Ingénierie Système 2020; S8140 v2. *https://doi.org/10.51257/a-v2-s8140*

[39] Wolfhard L, CAN System Engineering: From Theory to Practical Applications. Springer London; 2013.

[40] Ziegler J G, Nichols N B. Optimum Settings for Automatic Controllers. Transactions of the ASME 1942; 64(8):759–68.

[41] Åström K J, Murray R M. Feedback Systems: An Introduction for Scientists and Engineers. 1st ed. Princeton University Press; 2008.

[42] Ventura G, Risegari L. The Art of Cryogenics: Low-Temperature Experimental Techniques. 1st ed. Elsevier Science; 2008.

[43] Fagnard J-F, Vanderheyden B, Vanderbemden P. Magnetic shielding with bulk high temperature superconductors: factors influencing the magnetic field penetration in hollow cylinders. In : Muralidhar Miryala editor. *Superconductivity: recent developments and new production technologies*. Nova Science Publishers; 2012.

[44] Callaghan E E, Maslen S H, The magnetic field of a finite solenoid. Nasa Tech. Note 1960, no. D-465.

[45] Levin G A, Barnes P N, Murphy J, Brunke L, Long J D, Horwath J, Turgut Z. Persistent Current in Coils Made Out of Second Generation High Temperature Superconductor Wire. Appl Phys Lett 2008; 93(6):062504. *https://doi.org/10.1063/1.2969798*

[46] Lee H-G, Kim J G, Lee S W, Kim W S, Lee S W, Choi K D, Hong G W, Ko T K. Design and Fabrication of Permanent Mode Magnet by Using Coated Conductor. Physica C 2006; 445-448:1099–1102. *https://doi.org/10.1016/j.physc.2006.05.044*

[47] Wéra L, Fagnard J F, Levin G A, Vanderheyden B, Vanderbemden P. Magnetic Shielding with YBCO Coated Conductors: Influence of the Geometry on Its Performances. IEEE Trans Appl Supercond 2013; 23(3):8200504. *https://doi.org/10.1109/TASC.2012.2235514*

[48] Sheng J, Zhang M, Wang Y, Li X, Patel J, Yuan W. A New Ring-Shape High-Temperature Superconducting Trapped-Field Magnet. Supercond Sci Technol 2017; 30(9):094002. *https://doi.org/10.1088/1361-6668/aa7a51*

[49] Zheng Y, Wang Y, Li J, Jin Z. Magnetization of the Joint-Free High Temperature Superconductor (RE)$Ba_2Cu_3O_x$ Coil by Field Cooling. AIP Adv 2017; 7(9):095218. *https://doi.org/10.1063/1.4998230*

[50] Ali M Z, Zheng J, Huber F, Zhang Z, Yuan W, Zhang M. 4.6 T Generated by a High-Temperature Superconducting Ring Magnet. Supercond Sci Technol 2020; 33(4):04LT01. *https://doi.org/10.1088/1361-6668/ab794a*

[51] Zhao C, Shi J, Sheng J, Chen W. Study on the Electromagnetic Characteristics of Ring-Shaped Superconducting Permanent Magnets for Medical Applications. Crystals 2022; 12(10):1438. *https://doi.org/10.3390/cryst12101438*

[52] Liao H, Yuan W, Zhang Z, Zhang M. Magnetization mechanism of a hybrid high temperature superconducting trapped field magnet. J Appl Phys 2023; 133:023902. *https://doi.org/10.1063/5.0133219*

[53] Carusone T C, Johns D, Martin K. Analog Integrated Circuit Design. 2nd ed. Wiley; 2011.

Appendix I: Calibration of the commercial IC Hall sensor at room temperature

The calibration of the commercial 3-axis IC Hall sensor at room temperature was carried out in two steps: (i) determine the sensitivity and typical uncertainty, (ii) define the metrics and characterize the offset, linearity, and hysteresis.

First part: Sensitivity and uncertainty

In order to calibrate the sensitivity of the Hall sensor, two coaxial air coils connected in series are used. These are referred to as the calibration coils. The B/I ratio at the centre of the calibration coils, measured using a precision gaussmeter (LakeShore, 475 DSP Gaussmeter, HMNA-2518-VR-HF sensor) is 9.046 mT/A. The calibration coils can generate a magnetic flux density $\mu_0 H_{\text{app}} = B_{\text{app}}$ up to ~ 100 mT, which is close to the linear range around ± 120 mT guaranteed by the manufacturer of the Hall sensor for each axis. The field uniformity is better than 0.1% for any off-centring of 3 mm in the median plane of the calibration coils. The calibration is carried out by injecting a DC current ramped up to 11 A and then cycled three times between + 11 A and -11A. The ramp uses steps of 1 A, lasting 10 s each, during which measurements are averaged. Using both increasing and decreasing current ramps allows detecting a possible hysteresis in the magnetic components (e.g., magnetic field concentrator) embedded in the package of the Hall sensor.

Figure A1(a) shows the calibration results of B_z as measured by the Hall sensor, after averaging, when the applied flux density $\vec{B}_{\text{app}}$ is directed along z. Before calibration, i.e., using the typical sensitivity announced by the manufacturer, the averaged data in red are obtained ('uncalibrated data'). Adjusting the sensitivity for each axis with respect to the applied field measured by the gaussmeter (green) results in the blue curve. Similar graphs to Fig. A1(a) can be obtained for the flux density measured along the x and y directions. It is of interest to examine the $\vec{B}$ components which are not aligned with $\vec{B}_{\text{app}}$, to check the alignment of the sensor and observe the influence of the background noise. For example, the B_y data when $\vec{B}_{\text{app}}$ is along z are shown in Fig. A1(b). For an applied flux density along $z \approx 100$ mT, one finds $B_y \approx 0.25$ mT.

In addition to the averaged data, Fig. A1 also shows associated error bars. The inset in Fig. A1(a) highlights that the ideal data (green) effectively lies within the error bars. Horizontally, these bars arise from the uncertainty associated to the applied field. An upper bound on this uncertainty can be estimated from approximate uncertainties on the measured voltage drop across the shunt used for the measurement of the current, the shunt resistance and the calibrated B/I ratio. This computation is simplified by assuming a

maximum misalignment of 5° between the gaussmeter and the coil axis during the calibration of B/I. Consequently, the uncertainty associated to B_{app} roughly evolves linearly with the applied current I. Vertically, the error bars associated to B (measured by the Hall sensor) arise from the standard deviation of the B measurements for a certain applied field. For each value of the applied field, the distribution of the data around the mean value can be observed to be gaussian. The typical uncertainty is around ± 200 µT for x and y and ± 100 µT for z.

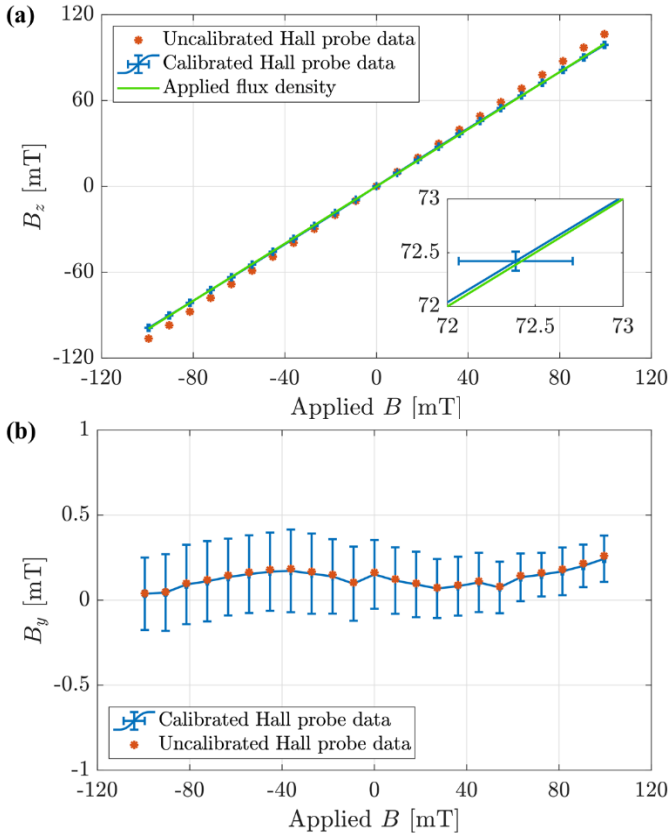

Fig. A1. (a) Measured and averaged B_z as a function of the applied flux density along z. Red: data before calibration of the sensitivity. Blue: data after calibration with respect to the B_z results for a calibrated gaussmeter (green). **(b)** Measured and averaged B_y as a function of the applied flux density along z. Red: data before calibration of the sensitivity. Blue: data after calibration with a calibrated gaussmeter (see text).

Second part: Offset, linearity and hysteresis

Then, the set of averaged data for B_x, B_y and B_z when $\vec{B}_{\text{app}}$ is aligned with each of the x, y and z directions can be used to estimate the offset, linearity and hysteresis of the Hall sensor. The metrics are as follows.

Offset #1. It is the average value of the magnetic flux density measured with no applied field, for each axis, irrespective of the orientation of the Hall sensor. Ideally, this offset should be computed in a zero-gauss chamber such that it does not depend on the Earth's field or other magnetic flux sources. TABLE A1 shows offset #1 values around the typical uncertainty level (a few hundred µT at most).

Offset #2. This way of computing the offset uses data for the B component aligned with the applied field (e.g. Fig. A1(a)). Within the linear range of the sensor, a first-order fitting can be performed to find the best straight line approximating the set of experimental data. It yields

$$B_{\text{fitted}}(B_{\text{app}}) = \alpha B_{\text{app}} + \beta,$$

where α is ideally equal to 1. Offset #2 is given by β, ideally equal to 0. This way of computing the offset is supposedly more reliable as it is based on more data points than offset #1. The computed offsets (TABLE A1) are even smaller in this case than in the previous one, which confirms the quality of the IC Hall sensor in terms of offset cancellation.

INL (Integral Non-Linearity). The INL is a common metric to assess the linearity of a converter [53]. The mathematical definition used here is slightly different from that used in some converters. Here, we define

$$\text{INL}_j = \max_{B_{\text{app}} \in \{-11k, -10k, \dots 11k\}} \left| B_{j,\text{fitted}}(B_{\text{app}}) - B_j(B_{\text{app}}) \right|,$$

for $j \in \{x, y, z\}$, where k is the B/I ratio, $B_{j,\text{fitted}}(B_{\text{app}})$ is given by the above equation and $B_j(B_{\text{app}})$ is the j component of the (average) magnetic flux density measured for a certain applied field, when the j axis is aligned with the main field. In other words, it represents the maximal difference between the (average) measured flux density component aligned with $\vec{B}_{\text{app}}$ and the best linear fitting approximating these data. The values given in TABLE A1 show that the INL is around several hundreds of µT, while the considered range is around ± 100 mT, which highlights the linearity of the Hall sensor.

Hysteresis max/avg. The datasheet mentions a possible hysteresis of ~ 0.43 mT at most. In order to measure it (using an air coil), the average magnetic flux density component aligned with $\vec{B}_{\text{app}}$ is computed for each applied field during an increasing ramp and during a decreasing ramp. The maximal difference between the 'increasing' and 'decreasing' measured flux density at a given applied field is then computed. Similarly, the average of this difference is taken over the different applied fields. Mathematically, it is described by

$$\begin{aligned} \Delta B_j &= B_j^{\nearrow}(B_{\text{app}}) - B_j^{\searrow}(B_{\text{app}}), \\ \text{Hyst max}_j &= \max_{B_{\text{app}} \in \{-11k, -10k, \ldots 11k\}} |\Delta B_j|, \\ \text{Hyst avg}_j &= \frac{1}{21} \sum_{B_{\text{app}} \in \{-11k, -10k, \ldots 11k\}} \Delta B_j, \end{aligned}$$

for $j \in \{x, y, z\}$, where k is the B/I ratio and $B_j^{\nearrow}(B_{\text{app}})$ (resp. $B_j^{\searrow}(B_{\text{app}})$) is the j component of the (average) magnetic flux density measured for a certain applied field during an increasing (resp. decreasing) current ramp, when the j axis is aligned with the main field. The results show that no real hysteresis is detected in these experiments, as the maximum hysteresis is less than twice the typical uncertainty level and the average hysteresis is even smaller.

TABLE A1: Metrics (Approximate Values) Assessing the Quality of the Hall Sensor in Terms of Offset, Linearity and Hysteresis.

Direction		x	y	z
Offset #1	[µT]	227	116	32
Offset #2	[µT]	2	134	1
INL	[µT]	615	499	658
Hysteresis max	[µT]	279	321	336
Hysteresis avg	[µT]	97	174	106

In summary, the main results from the above analysis are that (i) the measured offsets are small and of the order of the typical uncertainty, (ii) the integral non-linearity of the Hall sensor response over a 100 mT measurement range is less than 700 µT, and (iii) no hysteresis whose amplitude exceeds the typical uncertainty level is observed. Also, no significant difference is detected between the results for the three cycles of injected current.

A further set of experiments is carried out to determine the effective linear range of the sensor. While the manufacturer announces that the linear range is limited to ± 120 mT, flux density measurements up to ~ 300 mT along the x and y axes appear to saturate at ± 159 mT while those along the z axis are digitally limited (all bits at 1) at ± 217.5 mT.

Appendix II: Temperature dependence of the characteristics of the IC 3-axis Hall sensor

Before designing the temperature controller, it is necessary to highlight a possible influence of the temperature on the Hall sensor specifications. This possible temperature dependence can then be used to design the temperature controller.

The Hall sensor specifications from the manufacturer are given at 35°C. Therefore, the possible relative variations with respect to those at 35°C are studied as a function of temperature, using and air coil fed with a current ramp. Keeping the ramp duration less than 2 minutes enables a minimal heating due to the Joule effect in the coil. In order to quantify the temperature dependence of the signal for the three directions simultaneously, the Hall sensor is oriented in such a way that it measures a non-zero flux density for each axis. This setup is then placed in a climatic chamber whose temperature is controlled to be, successively, 5°C, 15°C, ..., 65°C. The relative humidity is kept constant throughout the experiments (50 %).

For each axis of the sensor and for each temperature, we obtain a set of measured B values as a function of the applied current. Fitting a first-order law on these data allows us to find the B/I ratio for each axis and temperature. Taking the one at 35°C as a reference, we then normalize the B/I ratios with respect to it. Then, we plot these normalized ratios as a function of temperature. It corresponds to the normalized sensitivity of the sensor, as the B/I ratio of the magnetizing coil is assumed unchanged. We compute the Pearson correlation coefficient as well as the slope of the best straight line fitting the evolution of the sensitivity with temperature. These two metrics are given for each axis in TABLE A2. In addition to the normalized sensitivity, the normalized offset (i.e., set to 0 mT at 35°C) is computed and plotted against the temperature, in order to extract the correlation coefficient and the slope of the best fitting line (TABLE A2). The way this offset is obtained, for each axis and for each temperature, is by taking the average between offset #1 and #2, following the definitions given in the section above.

TABLE A2: Metrics (Approximate Values) Assessing the Influence of the Temperature on the Normalized Hall Sensor Specifications.

Direction		x	y	z
Sensitivity: correlation	[-]	0.13	−0.27	0.85
Sensitivity: slope	[$\times 10^{-4}$ K^{-1}]	1.93	−5.39	3.69
Offset: correlation	[-]	−0.97	0.84	0.46
Offset: slope	[μT K^{-1}]	−12.2	14.5	1.6

The main conclusion of this experiment is that no significant variation of the specifications can be observed as a function of the temperature. Either the correlation coefficient is poor, or the slope is very low. The conclusion to be drawn is that small temperature variations of a few degrees, e.g., arising from the temperature control inside the experimental chamber, have practically no influence on the measurement, as they induce a change much smaller than the typical uncertainty level.

Appendix III: Tasks run by the microcontroller

The microcontroller is programmed such that it runs (except if an error state is triggered) the following tasks continuously.

1. Every 5 ms, the microcontroller asks the Hall sensor, via SPI, to perform a flux density and a temperature measurement. The status of the sensor is checked to ensure the correct reception of the request.

2. Then, 2 ms later, the Hall sensor data (B_x, B_y, B_z and temperature) are read and verified (status of the sensor and cyclic redundancy check).

3. Once 100 measurements have been performed without any error detected, the averaged data are sent to the computer via CAN bus.

4. Every second, the microcontroller reads the Pt100 voltage drop (via the microcontroller Analog-to-Digital Converter (ADC)).

5. Every second, just after the ADC reading, the Pt100 temperature is sent to the computer and the temperature control is performed.